materials

MDPI

Article

Improved Methane Production by Photocatalytic CO_2 Conversion over $Ag/In_2O_3/TiO_2$ Heterojunctions

Patricia Reñones †, Fernando Fresno *,†, Freddy E. Oropeza and Víctor A. de la Peña O'Shea *

Photoactivated Processes Unit, IMDEA Energy, Avda. Ramón de la Sagra 3, 28935 Madrid, Spain; patricia.renones@csic.es (P.R.); freddy.oropeza@imdea.org (F.E.O.)

* Correspondence: fernando.fresno@csic.es (F.F.); victor.delapenya@imdea.org (V.A.d.l.P.O.)

† Present address: Instituto de Catálisis y Petroleoquímica, CSIC, C/Marie Curie 2, 28049 Madrid, Spain.

Abstract: In this work, the role of In_2O_3 in a heterojunction with TiO_2 is studied as a way of increasing the photocatalytic activity for gas-phase CO_2 reduction using water as the electron donor and UV irradiation. Depending on the nature of the employed In_2O_3, different behaviors appear. Thus, with the high crystallite sizes of commercial In_2O_3, the activity is improved with respect to TiO_2, with modest improvements in the selectivity to methane. On the other hand, when In_2O_3 obtained in the laboratory, with low crystallite size, is employed, there is a further change in selectivity toward CH_4, even if the total conversion is lower than that obtained with TiO_2. The selectivity improvement in the heterojunctions is attributed to an enhancement in the charge transfer and separation with the presence of In_2O_3, more pronounced when smaller particles are used as in the case of laboratory-made In_2O_3, as confirmed by time-resolved fluorescence measurements. Ternary systems formed by these heterojunctions with silver nanoparticles reflect a drastic change in selectivity toward methane, confirming the role of silver as an electron collector that favors the charge transfer to the reaction medium.

Keywords: photocatalysis; CO_2; heterojunction; titanium dioxide; indium dioxide; artificial photosynthesis

Citation: Reñones, P.; Fresno, F.; Oropeza, F.E.; de la Peña O'Shea, V.A. Improved Methane Production by Photocatalytic CO_2 Conversion over $Ag/In_2O_3/TiO_2$ Heterojunctions. *Materials* **2022**, *15*, 843. https://doi.org/10.3390/ma15030843

Academic Editors: Simona Bennici and Ilenia Rossetti

Received: 29 December 2021
Accepted: 20 January 2022
Published: 22 January 2022

1. Introduction

Currently, the scientific community is putting a great deal of effort into the search for clean fuels, in order to reduce the continuous CO_2 emissions to the atmosphere and face the depletion of fossil fuels, which, together, cause the emerging energy and environmental global crises. A promising alternative to reduce the CO_2 concentration in the atmosphere and to convert it into renewable fuels or chemicals is so-called artificial photosynthesis [1–5]. This process is based on the photoreduction of CO_2 using H_2O as an electron donor and solar light as energy source. The most studied catalyst for this reaction, similarly to other photocatalysis applications, is TiO_2 because of its low cost, nontoxicity, (photo)chemical stability, and high activity relative to other semiconductors. However, TiO_2 presents some disadvantages which limit its efficiency; it is only active under UV light and the photogenerated electron–hole pairs recombine with a high rate. In the last few years, researchers have been developing different strategies of modification to enhance the photocatalytic performance of TiO_2, such as the use of dopants, cocatalysts, heterojunctions, single active sites, and bandgap engineering [6–14]. Among them, the formation of heterojunctions shows great potential because of its versatility and its effectiveness in reducing the recombination of electron–hole pairs, thus improving the charge separation and enhancing photocatalytic performance [9,15–18]. Furthermore, the use of heterojunctions can also enhance the light harvesting and extend the light absorption toward the visible range by means of a sensitization mechanism [16,19–24]. There are some kinds of heterojunctions, based on the use of inorganic semiconductors, which present higher activity than bare TiO_2 in different photocatalytic applications, such as La_2O_3/TiO_2, In_2O_3/TiO_2, Fe_2O_3/TiO_2,

SnO_2/TiO_2, and V_2O_5/TiO_2, which promote charge separation and transfer, improve the light harvesting, or modify the surface chemistry of the system [25,26]. In addition, there is the possibility of creating three-component or ternary systems based on the union of oxides with a metal, thus allowing more efficient charge transfer and adding additional catalytically active sites [27–31].

In this work, the role of In_2O_3 in a heterojunction with TiO_2 is studied as a way of increasing the photocatalytic activity for CO_2 reduction [32–36]. This oxide was chosen due to the fact that its conduction and valence band energy levels are in proper places to be combined with TiO_2 for promoting the migration of photoexcited electrons, which can effectively enhance the separation of electron–hole pairs and the interfacial charge transfer [37,38]. Different kinds of heterojunctions of In_2O_3 with commercial TiO_2 (anatase) were synthesized while changing the particle size of the In_2O_3 particles, by using a commercial In_2O_3 and In_2O_3 synthesized in the laboratory, with the aim of studying the role of the size of the In_2O_3 particles in the properties of the catalysts and in their photocatalytic behavior [3,12,27]. Furthermore, ternary systems based on the In_2O_3/TiO_2 heterojunctions and silver nanoparticles were synthesized to further enhance the charge extraction and transfer with respect to TiO_2 and binary catalysts. Silver was selected because of its ability to improve the selectivity toward highly electron-demanding products such as methane [6,39].

2. Materials and Methods

2.1. Preparation of Catalysts

In all cases, the TiO_2 employed was a commercial anatase-type titanium dioxide (TiO_2, PC500) supplied by CristalACTIV^{TM} (Thann, France) In the first series of catalysts (c-series), commercial In_2O_3, supplied by Across Organics (Geel, Belgium), was used for the formation of the heterojunctions with TiO_2. For the preparation of the mixed oxides, appropriate amounts of each of them for a final content of 1, 5, and 10 wt.% In_2O_3 were suspended in 10 mL of Milli-Q water. The suspension was then treated in an ultrasonic bath for 1 h, and the water was eliminated by evaporation at 100 °C. Afterward, the samples were ground in an agate mortar, calcined in air at 400 °C for 4 h with a temperature ramp of 10 °C/min, and finally ground again. This temperature was chosen in order to eliminate any possible organic impurity while avoiding the phase change of TiO_2 from anatase to rutile [8,39]. The catalysts were labeled as xIn_2O_3-c/TiO_2, where x indicates the nominal In amount in wt.%. For the second series (p-series), In_2O_3 was prepared in the laboratory using $In(NO_3)_3 \cdot xH_2O$ as a precursor, provided by Sigma-Aldrich (Darmstadt, Germany). The amount of the precursor required for the desired amount of In_2O_3 was dissolved in 72 mL solution of ethanol and water (3/1); then, the solvents were evaporated in a rotatory evaporator, and the obtained powder was dried at 100 °C overnight. The collected powder was calcined at 250 °C for 3 h with a temperature ramp of 10 °C/min and finally ground in an agate mortar, obtaining the sample named In_2O_3-p. This temperature was chosen since, according to Hoch et al. [37], it maximizes the formation of surface oxygen vacancies and hydroxyl groups, being the material most active. Then, the formation of the heterojunction between TiO_2 and In_2O_3-p was performed, following the method described above for xIn_2O_3/TiO_2 heterojunctions, and labeling the samples xIn_2O_3-p/TiO_2, where x indicates the nominal In amount in wt.%.

Silver was incorporated by wet impregnation. The necessary amount of $AgNO_3$ (Sigma Aldrich, Darmstadt, Germany) for 1 wt.% Ag was dissolved in 25 mL of Milli-Q water, and then TiO_2 was suspended in this solution. Then, the water was eliminated in a rotatory evaporator and the powder was dried in an oven at 100 °C overnight. Afterward, the solid was ground and calcined at 400 °C for 4 h with a temperature ramp of 5 °C/min, before grinding again. Then, the formation of the heterojunction between Ag/TiO_2 and In_2O_3 (In_2O_3-c or In_2O_3p) was performed, following the method described above for xIn_2O_3-c/TiO_2 and xIn_2O_3-p/TiO_2 heterojunctions.

2.2. Characterization

X-ray diffractograms were registered with a Panalytical EMPYREAN equipment (Malvern, UK) using Cu Kα radiation (λ = 1.54178 Å) with a scanning rate of $0.01^{\circ}\cdot s^{-1}$. The average crystal size was estimated by applying the Scherrer equation to the most intense diffraction peak of each phase. Pawley refinements were realized with the X'Pert High Score Plus software (version 2.2.1, Panalytical, Malvern, UK) for the calculation of cell parameters. Metal quantification was carried out by ICP-OES with a Perkin Elmer Optima3300 DV spectrometer (Waltham, MA, US) BET surface areas were estimated from N_2 adsorption/desorption isotherms measured at 77 K using a QUADRASORB instrument (Quantachrome Instruments, Boynton Beach, FL, US) after degassing the samples under nitrogen at 105 °C for 20 h. Morphological properties were analyzed using a transmission electron microscope (TEM) JEOL 2100F with an energy-dispersive X-ray (EDX) detector from Oxford Instruments (Abingdon, UK) for chemical microanalysis. UV/Vis diffuse reflectance spectra were recorded in a Perkin Elmer Lambda 1050 spectrometer (Waltham, MA, USA) between 250 and 800 nm, taking $BaSO_4$ as a 100% reflectance reference. Tauc plots were used to estimate optical bandgaps. Fluorescence spectra were recorded with a Perkin Elmer LS55 spectrometer (Waltham, MA, US), setting the excitation wavelength at 300 nm and filtering the emission below 350 nm. For the measurement of fluorescence lifetime, exponential decay curves were fitted to fluorescence decay data obtained by time-correlated single photon counting (TCSPC) with a Mini-τ device from Edinburgh Instruments (Livingston, UK), using as an excitation source a pulsed laser with 372 nm emission wavelength, 1 MHz pulse frequency, and 61.2 ps pulse width, and selecting a fluorescence emission of 450 $\pm$ 25 nm by means of a bandpass filter. X-ray photoelectron spectra (XPS) were taken in a SPECS spectrometer (Berlin, Germany), with an Al K_α X-ray source monochromated at 1486.6 eV and a PHOIBOS 150 NAP 1D-DLD analyzer. The pass energy was selected as 40 eV for survey scans and 20 eV for high-resolution scans. The binding energy scale was set using Au $4f_{7/2}$ (84.01 eV) and Ag $3d_{5/2}$ (368.20 eV). The spectra, recorded with charge compensation, were further calibrated using the C 1*s* signal of adventitious carbon. Casa XPS software (version 2.3. 24, Casa Software Ltd., Devon, UK) was used for data analysis, where Shirley or two-point linear background types were employed. Surface chemical compositions were determined using peak areas and Casa XPS sensitivity factors (C 1*s* RSF = 1.000).

2.3. Photocatalytic CO_2 Reduction

Gas-phase photocatalytic CO_2 reduction reactions were carried out in a continuous 280 mL stainless-steel reactor provided with a borosilicate glass window. Glass microfiber filters were coated with the powdered catalysts (100 mg) from a suspension in Milli-Q water and fitted into the reactor, so that the reacting gas, composed of CO_2 (99.9999%, Praxair, Madrid, Spain) and Milli-Q water mixed in a molar ratio of 7.25 with a controlled evaporation and mixing system (CEM, Bronkorst, Ruurlo, Netherlands), flew through the filter. The reaction pressure was 2 bar, and the reaction temperature was 50 °C. Four Philips Actinic lamps (λ_{max} = 365 nm, 6 W each, Amsterdam, Netherlands) were used for UV irradiation, with a total irradiance of 50 $W\cdot m^{-2}$ between 330 and 400 nm, as measured with a StellarNet BLUE-Wave spectrometer (Tampa, FL, USA).

In a typical procedure, a cleaning step of 5 min in vacuum and 1 h flushing with 100 mL/min Ar were carried out. After that, an adsorption/desorption equilibration step with 30 mL/min of the reacting gas took place. Then, the reactor was pressurized, the total flow was set to 2 mL/min, and the outlet gas was analyzed in line in the dark with a gas chromatograph (Agilent 7890, MS5A, Q-PLOT and CP-Sil5B columns, two FID and one TCD detectors, Santa Clara, CA, US). One hour later, the UV source was switched on, and the reaction was allowed to proceed for 15 h. Results are expressed as the total amount of product obtained after 15 h, while C-selectivity (carbon selectivity) to methane is defined as the amount of methane produced divided by the total amount of carbon-containing products.

3. Results and Discussion

3.1. Materials Characterization

Table 1 collects the main physicochemical characteristics of the prepared catalysts. Chemical analyses by ICP-OES revealed that the indium and silver concentrations in the heterojunctions were in the range of the nominal ones. Further surface chemical analyses based on XPS also revealed a close agreement with the nominal concentration of the samples, thus confirming a homogeneous distribution of the In_2O_3–TiO_2 heterojunction.

Table 1. Main physicochemical characteristics of the studied catalysts.

Catalyst	Bulk In (wt.%) [a]	Surface In (wt.%) [b]	Bulk Ag (wt.%) [a]	Surface Ag (wt.%) [b]	S_{BET} (m^2/g)	In_2O_3 Crystallite Size (nm)	TiO_2 Cell Parameters (Å)	
							a = b	c
TiO_2	-	-	-	-	112	-	3.7844	9.5088
$1In_2O_3$-c/TiO_2	1.11 ± 0.06	1.3	-	-	121	105	3.7836	9.5072
$5In_2O_3$-c/TiO_2	4.6 ± 0.2	4.0	-	-	119	68	3.7839	9.508
$10In_2O_3$-c/TiO_2	9.1 ± 0.5	9.5	-	-	115	83	3.7826	9.5094
$1In_2O_3$-p/TiO_2	0.89 ± 0.04	0.7	-	-	101	13	3.7811	9.5082
$5In_2O_3$-p/TiO_2	4.0 ± 0.2	n.m.	-	-	104	15	3.7849	9.5106
$10In_2O_3$-p/TiO_2	9.4 ± 0.4	10.5	-	-	100	16	3.7838	9.508
Ag/$1In_2O_3$-c/TiO_2	0.73 ± 0.04	n.m.	0.76 ± 0.04	3.1	109	78	3.7839	9.5079
Ag/$1In_2O_3$-p/TiO_2	0.73 ± 0.04	n.m.	0.79 ± 0.04	2.3	90	16	3.7841	9.5076

[a] From ICP-OES. [b] From XPS in the Ti 2*p* and In 3*d* regions and respective sensitivity factors. n.m.: not measured.

XRD diffraction patterns (Figure 1) exhibited in both series the characteristic diffraction peaks of In_2O_3 (ICDD-PDF: 01-071-2195) and anatase TiO_2 (ICDD-PDF: 01-084-1286) as the only crystal phases. Pawley refinements were carried out to compare the TiO_2 lattice cell parameters with those of bare TiO_2 (Table 1). The calculated cell parameters of all In_2O_3-loaded TiO_2 samples were in agreement with those of bare TiO_2, corroborating the formation of a composite material instead of a possible doping. The crystal sizes, determined by the Scherrer equation (Table 1), were higher for commercial In_2O_3 than for In_2O_3-p particles, around 80 and 14 nm, respectively. In the case of TiO_2 particles, the anatase crystal size (not shown) presented only small, nonsignificant variations in all heterojunctions with respect to bare titania. For ternary catalysts, the In_2O_3 and TiO_2 phases were observed, but there were no signs of metallic silver or silver oxide phases (see Supplementary Material, Figure S1). This can be traced back to the crystal size and/or total amount of Ag phases lower than the detection limits of the technique. XPS spectra of Ag-loaded samples in the Ag 3*d* region (Figure S2), in turn, could be fitted with a pair of symmetric Voigt functions at 368.6 eV and 374.6 eV. The symmetry of the peaks and the absence of satellite peaks (characteristic for metallic Ag) indicate that silver was in the oxide state. Although as-prepared samples contained Ag oxides, such species underwent reduction under reaction conditions, leading to metallic Ag as the actual cocatalyst for the CO_2 reduction [6,39]. According to ICP and XPS chemical analyses (see results in Table 1), the Ag surface fraction was 3.1 and 2.3 wt.% for Ag/$1In_2O_3$-c/TiO_2 and Ag/$1In_2O_3$-p/TiO_2, respectively. Provided that silver was only decorating the TiO_2 surface, the higher Ag concentration in the c-series catalyst may have resulted from lower surface interaction with In_2O_3 particles due to the higher crystallite size of the commercial In_2O_3 sample [6,8,39].

The Raman analysis of all materials showed the signals of TiO_2 anatase (Figure S3) (143 (E_g), 196 (E_g), 396 (B_{1g}), 516 (A_{1g} + B_{1g}), and 639 cm^{-1} (E_g)) [40,41], while no signals corresponding to In_2O_3 (133 (E_{2g}), 303 (E_{1g}), 336 (E_{2g}), 495 (A_{1g}), and 629 cm^{-1} (E_{2g})) [42,43] were identified. Only a small shift in the most intense peak of anatase (143 cm^{-1}, E_g) [37,44] was observed, which could be related to the presence of the most intense peak of In_2O_3, as observed in the individual Raman spectra of In_2O_3 samples in Figure S2c.

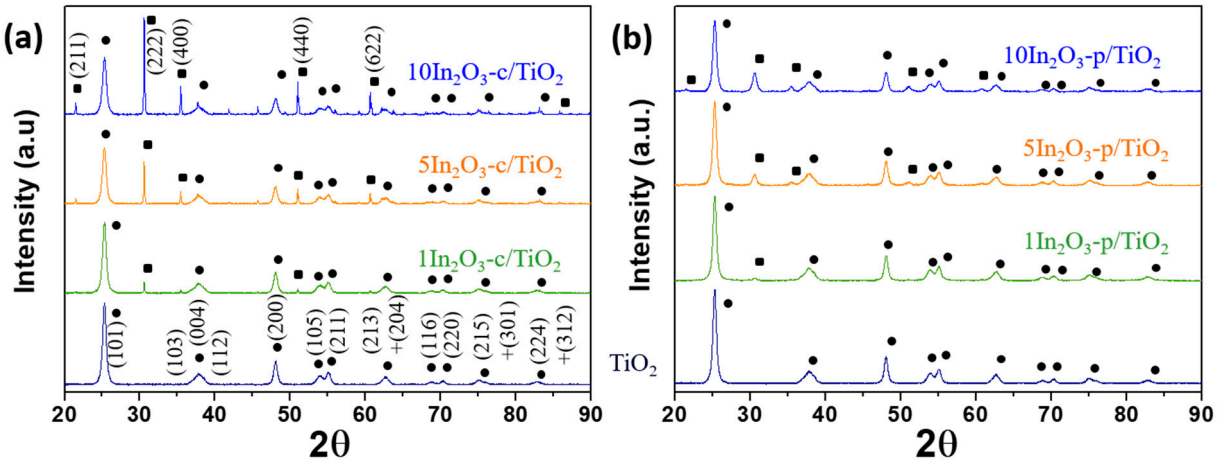

Figure 1. X-ray diffractograms of (**a**) c-series and (**b**) p-series catalysts. The identified phases are differentiated with symbols: •TiO_2 (ICCD-PDF: 01-084-1286) and ■ In_2O_3 (ICCD-PDF: 01-071-2195), and their Miller indices are included.

Regarding textural properties (Table 1), for the p-series, a reduction in surface area occurred with the inclusion of indium oxide compared to TiO_2, and this became more significant with the growth of In_2O_3 percentage. This could be related to the small size of In_2O_3-p particles that can enter the interparticle pores of TiO_2. On the other hand, the c-series catalysts, which contain larger In_2O_3 crystallites, showed a slight increase in the surface area compared to TiO_2. This probably occurred due to the higher crystal size of In_2O_3 particles, whereby they could not enter the interparticle pores of TiO_2, avoiding the agglomeration of the particles. In all ternary systems, the area was decreased with respect to unmodified TiO_2 and to the corresponding binary systems, which could be ascribed to partial obstruction of TiO_2 pores by silver nanoparticles (Table 1) [6,39].

Figure 2 shows the TEM images of 1% In catalysts in both series. In both cases, the TEM analysis showed a good dispersion of the In_2O_3. EDX analysis confirmed that the particles with darker contrast corresponded to In_2O_3. Furthermore, the amounts of In corresponded well with the nominal value in all analyzed samples (Figure S4).

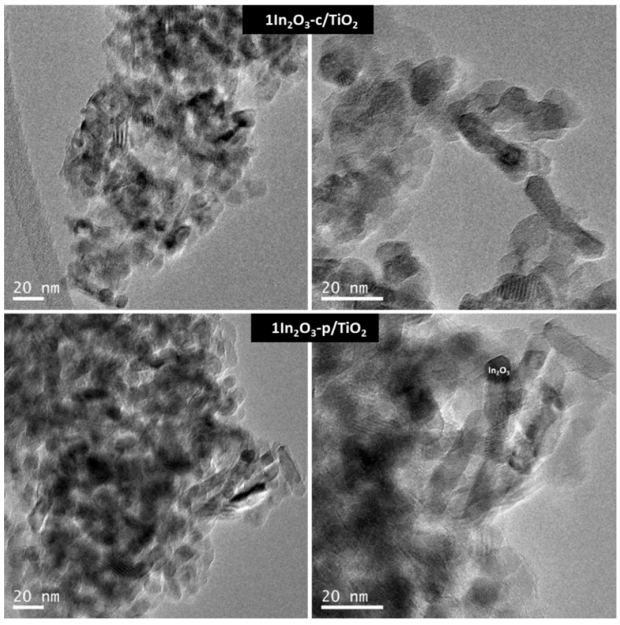

Figure 2. TEM micrographs of $1In_2O_3$-c/TiO_2 and $1In_2O_3$-p/TiO_2 catalysts.

UV/Vis diffuse reflectance spectra (Figure 3) show that, in both c- and p-series, the presence of indium oxide led to increased absorption in the visible range, which increased with the In_2O_3 content and could be associated with the bandgap transition of indium oxide (2.6 eV for both commercial and synthesized In_2O_3). Deconvolution of TiO_2 and In_2O_3 contributed to the spectra as an optical bandgap for the former of 3.1 eV in all doped samples, the same values as in bare TiO_2, in agreement with the deduced formation of a heterojunction rather than doping. In the case of ternary catalysts, which were UV-irradiated before acquiring the spectra, the absorption generated by the surface plasmon resonance of silver particles was also observed.

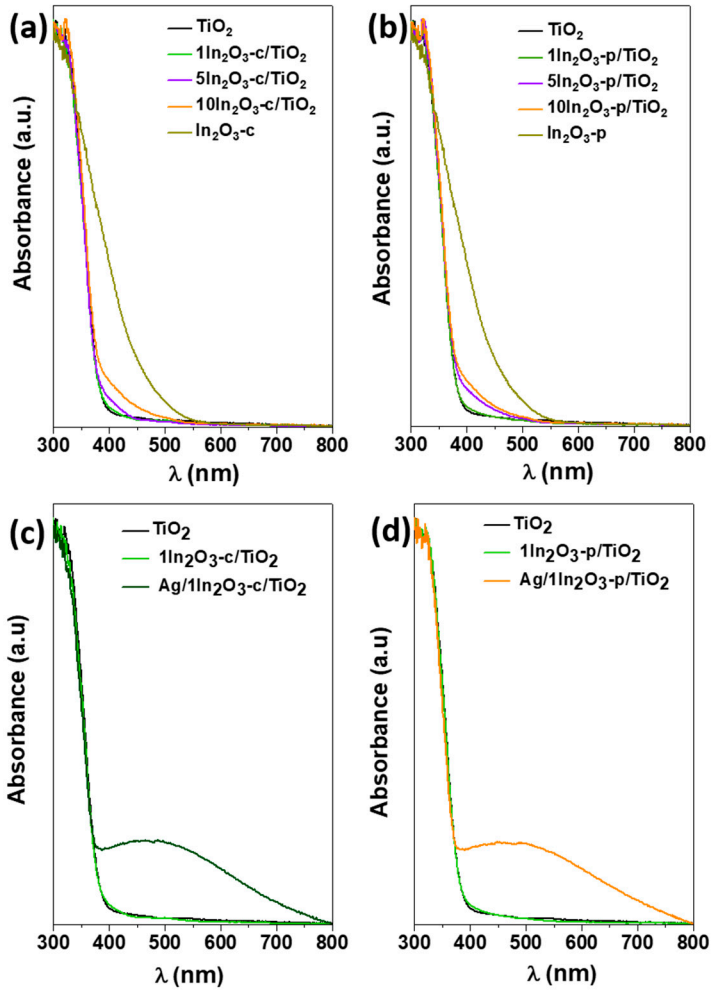

Figure 3. UV/Vis diffuse reflectance spectra of all catalysts studied compared to TiO_2: (**a**) c-series, (**b**) p-series, and (**c**,**d**) ternary catalysts compared to their binary counterparts.

Steady-state fluorescence spectra (Figure S5) show that emission wavelengths essentially matched those of TiO_2 in all cases, indicating that the photoluminescence contribution of In_2O_3 was minimal, as could be expected from the low concentration of In_2O_3 in the studied samples. However, a decrease in the emission in comparison with bare TiO_2 was observed, which may indicate a reduction in the recombination rate of electrons and holes [21,45–47] and, therefore, a charge transfer between phases. To confirm this, fluorescence lifetime measurements were carried out (Figure 4). Time-resolved spectra revealed an increased fluorescence lifetime in heterojunctions associated with electron transfer from In_2O_3 to TiO_2, according to their relative band positions, with the conduction band of the indium oxide at higher energy that that of titania [37,38], such that electrons could migrate from the former to the latter; thus, the duration of the fluorescence emission increased [48].

In the c-series, this transfer increased from 0 to 1 to 5 wt.% In_2O_3, but decreased with 10 wt.%, suggesting that the contact between both phases was no longer efficient with high In_2O_3 amount. In the p-series, however, the transfer continued being efficient up to 10 wt.%, which could be traced back to an improved phase contact due to the smaller size of In_2O_3 crystallites [22,28,46]. The case of silver-containing catalysts was more complex, as results revealed opposite effects. On the one hand, as described above, In_2O_3 transferred electrons to the conduction band of titania, increasing fluorescence lifetime; on the other hand, silver withdrew charge from the TiO_2 conduction band [6], decreasing lifetime. As a result, the value obtained for $Ag/1In_2O_3/TiO_2$, whatever the series, was similar to or slightly lower than in $1In_2O_3/TiO_2$.

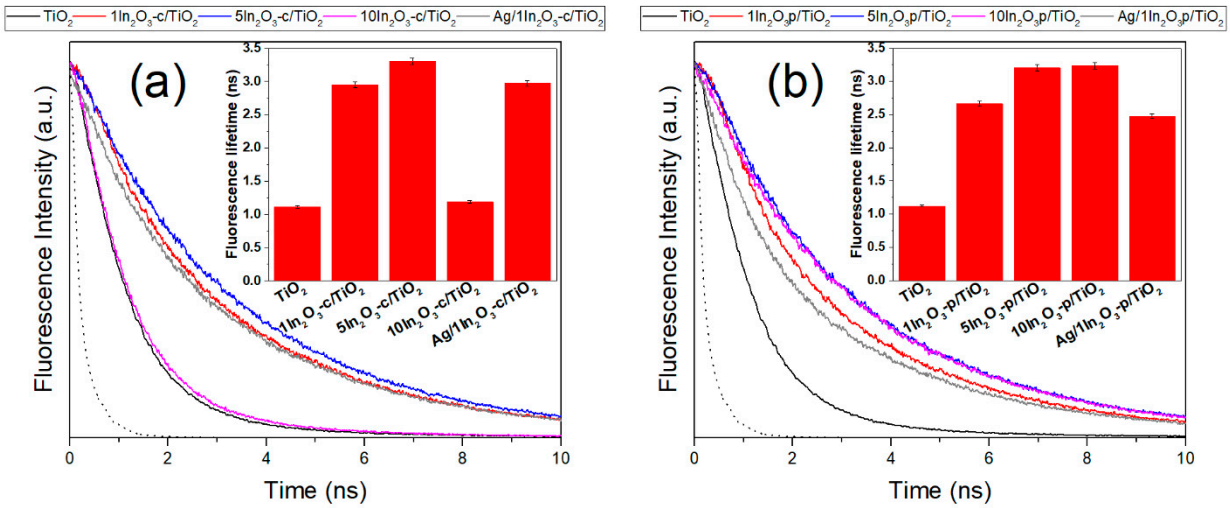

Figure 4. Fluorescence decay curves (main graphs) and fluorescence lifetimes obtained from fittings (insets), for the c-series (**a**) and the p-series (**b**) catalysts. Dotted lines represent the instrument response function.

3.2. Photocatalytic Tests

Figure 5 represents, in the left panel, the amounts of the different products obtained in CO_2 photoreduction over the studied catalysts after 15 h of irradiation. Bare TiO_2 gave rise to CO as the main product, with minor amounts of CH_4, CH_3OH, and C_2 (ethylene and ethane), together with hydrogen resulting from the parallel reduction of water. The incorporation of In_2O_3 led to changes in the product distribution with an increase in CH_4 and H_2 production in both In_2O_3/TiO_2 series, which was higher for larger amounts of In loading. This enhancement was higher in the case of the p-series, with a more than sevenfold increase in produced CH_4 for the $10In_2O_3$-p$/TiO_2$ catalyst with respect to TiO_2. These changes were also combined with a slight increase in C_2 and a decrease in CO production. Regarding In_2O_3, the obtained methane production was ca. 46%, obtained with TiO_2. Therefore, improved methane production was in all cases higher than the linear combinations of the activities of the single components, revealing a synergistic effect.

This change in product distribution was previously observed and attributed to a decrease in the electron–hole recombination rate that favors the formation of highly electron-demanding products [1,49,50]. Among these products, selectivity to methane is most affected by the catalyst nature, while that to methanol and C_2 is essentially maintained upon introduction of indium oxide. Focusing, therefore, on methane selectivity, the right panel of Figure 5 shows the values obtained with the different catalysts, considering only the carbon products as indicated in the experimental section. The graph allows observing a correlation between selectivity to methane and fluorescence lifetime (and, therefore, inter-phase charge transfer). Thus, in good accordance with the results shown in Figure 4, CH_4 selectivity increased in the c-series, from TiO_2 to $1In_2O_3$-c$/TiO_2$ and from this to $5In_2O_3$-c$/TiO_2$, and then the improvement was practically lost when using 10 wt.% In_2O_3. On the contrary, in

the p-series, the selectivity was also considerably higher when introducing 1% In_2O_3, before further increasing with 5%; however, there was a further improvement when the amount of indium oxide was increased to 10%, which could be traced back to the maintained charge transfer observed in time-resolved fluorescence measurements. Therefore, a direct effect of this charge transfer on the selectivity toward a highly electron-demanding product such as methane could be envisaged, and this effect was more pronounced with more extensive phase contact derived from smaller In_2O_3 crystallites.

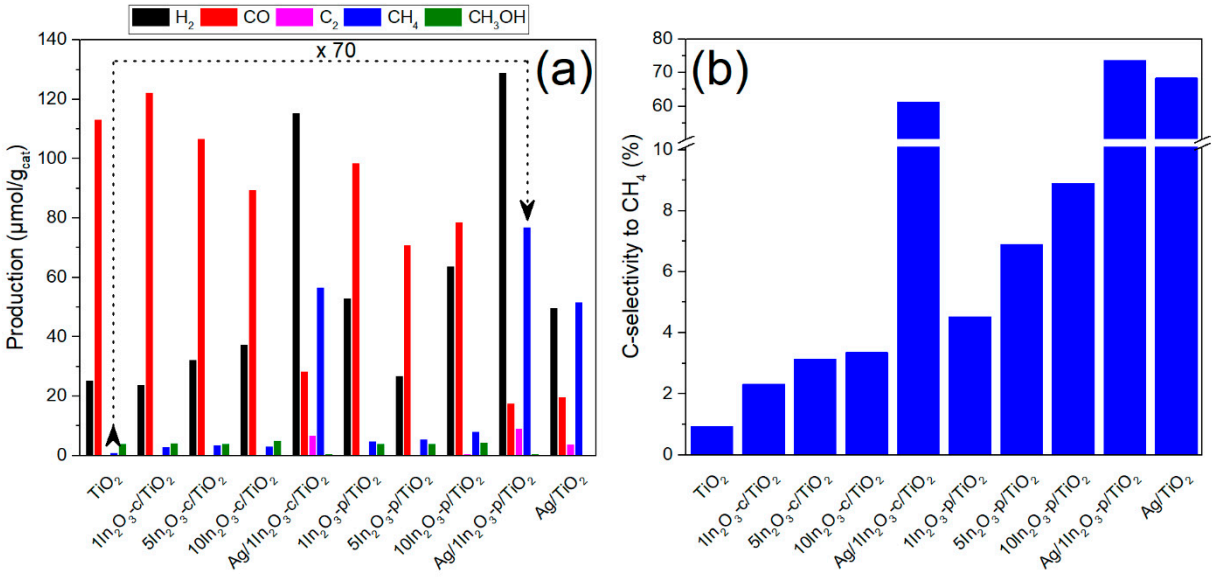

Figure 5. (**a**) Cumulative production of the main products obtained with different catalysts in the CO_2 + H_2O reaction after 15 h under UV light. (**b**) C-selectivities (%) toward CH_4 in the same reaction.

The effect of silver deposition on the reactivity and selectivity was studied with the 1% In_2O_3 samples in both c- and p-series. A great improvement in the selectivity toward CH_4 was observed in both series, being again particularly significant for the p-series sample, which improved the production of methane attained with TiO_2, $1In_2O_3$-p/TiO_2, and the previously reported [6] Ag/TiO_2 by 70, 15.5, and 1.5 times, respectively. This improved reactivity to methane was attributed to the electron-scavenging ability of Ag nanoparticles, which further increased electron ability for intensive CO_2 reduction into the eight-electron product CH_4 [6].

Lastly, it is worth noting that selectivity to hydrogen against carbon products, as deduced from Figure 5 (left), evolved in a similar way as that to methane across the different indium amounts and even with the introduction of the silver cocatalyst, subtracting photoexcited electrons from being used for CO_2 reduction. A further challenge with the present catalysts is, therefore, to drive the competition for conduction band electrons toward CO_2, thus pursuing total selectivity to methane.

4. Conclusions

With the heterojunctions based on In_2O_3 and TiO_2, better activities were obtained with respect to bare anatase TiO_2. This enhancement was reflected mostly in the selectivity to methane and was related to a decreased electron–hole recombination as confirmed by fluorescence analysis. The activity results also revealed a significant change depending on the crystal size of the In_2O_3 employed. The smaller crystallite size of indium particles obtained in the laboratory favored methane production, but gave a lower overall conversion than the bare TiO_2 and the heterojunctions formed between TiO_2 and commercial In_2O_3, suggesting that electrons were directed toward the eight-electron reduction product CH_4. Time-resolved fluorescence measurements allowed relating the improved methane selectiv-

ity to the transfer of photoexcited electrons from In_2O_3 to TiO_2, which was more efficient with smaller In_2O_3 catalysts. The ternary systems formed between Ag and In_2O_3/TiO_2 enabled a further increase in CH_4 production, with the ternary catalysts prepared with synthetic In_2O_3 again being more active than those with commercial In_2O_3. As a result, the best Ag/In_2O_3 system improved both CH_4 production and selectivity compared to the previously studied Ag/TiO_2 system, and it enhanced CH_4 production with respect to TiO_2 by a factor of 70.

Supplementary Materials: The following are available online at https://www.mdpi.com/article/10.3390/ma15030843/s1: Figure S1. X-ray diffractograms of the ternary catalysts; Figure S2. XPS in the Ag 3*d* region of $Ag/1In_2O_3$-p/TiO_2 and $Ag/1In_2O_3$-c/TiO_2; Figure S3. Raman spectra of (a) c-series, (b) p-series, (c) In_2O_3-c and In_2O_3-p, and (d) ternary photocatalysts, compared to TiO_2; Figure S4. EDX analysis by TEM of $1In_2O_3$-c/TiO_2 and $1In_2O_3$-p/TiO_2 photocatalysts; Figure S5. Fluorescence spectra of all catalysts.

Author Contributions: Conceptualization, P.R., F.F. and V.A.d.l.P.O.; methodology, P.R., F.F., and F.E.O.; validation, P.R., F.F., F.E.O. and V.A.d.l.P.O.; formal analysis, P.R., F.F., F.E.O., and V.A.d.l.P.O.; investigation, P.R., F.F., F.E.O. and V.A.d.l.P.O.; writing—original draft preparation, P.R. and F.E.O.; writing—review and editing, F.F. and V.A.d.l.P.O.; visualization, P.R., F.F., and F.E.O.; supervision, F.F. and V.A.d.l.P.O.; funding acquisition, V.A.d.l.P.O. All authors have read and agreed to the published version of the manuscript.

Funding: This research was funded by the European Union's Horizon 2020 research and innovation program under the European Research Council (ERC) through the HyMAP project, grant agreement No. 648319. Additional funding by the Spanish MCIN/AEI/10.13039/501100011033/FEDER through the Nympha Project (PID2019-106315RB-I00), the regional government of "Comunidad de Madrid" and the European Structural Funds through FotoArt-CM program (S2018/NMT-4367), and Fundación Ramón Areces through the ArtLeaf project is gratefully acknowledged.

Institutional Review Board Statement: Not applicable.

Informed Consent Statement: Not applicable.

Data Availability Statement: Not applicable.

Conflicts of Interest: The authors declare no conflict of interest.

References

1. Fresno, F.; Villar-Garcia, I.; Collado, L.; Alfonso González, E.; Reñones, P.; Barawi, M.; de la Peña O'Shea, V. Mechanistic View of the Main Current Issues in Photocatalytic CO_2 Reduction. *J. Phys. Chem. Lett.* **2018**, *9*, 7192–7204. [CrossRef] [PubMed]
2. Handoko, A.D.; Li, K.; Tang, J. Recent Progress in Artificial Photosynthesis: CO_2 Photoreduction to Valuable Chemicals in a Heterogeneous System. *Curr. Opin. Chem. Eng.* **2013**, *2*, 200–206. [CrossRef]
3. Ola, O.; Maroto-Valer, M.M. Review of Material Design and Reactor Engineering on TiO_2 Photocatalysis for CO_2 Reduction. *J. Photochem. Photobiol. C Photochem. Rev.* **2015**, *24*, 16–42. [CrossRef]
4. Bushuyev, O.S.; De Luna, P.; Dinh, C.T.; Tao, L.; Saur, G.; van de Lagemaat, J.; Kelley, S.O.; Sargent, E.H. What Should We Make with CO_2 and How Can We Make It? *Joule* **2018**, *2*, 825–832. [CrossRef]
5. Das, S.; Wan Daud, W.M.A. A Review on Advances in Photocatalysts towards CO_2 Conversion. *RSC Adv.* **2014**, *4*, 20856. [CrossRef]
6. Collado, L.; Reynal, A.; Fresno, F.; Barawi, M.; Escudero, C.; Perez-Dieste, V.; Coronado, J.M.; Serrano, D.P.; Durrant, J.R.; de la Peña O'Shea, V.A. Unravelling the Effect of Charge Dynamics at the Plasmonic Metal/Semiconductor Interface for CO_2 Photoreduction. *Nat. Commun.* **2018**, *9*, 4986. [CrossRef]
7. Reñones, P.; Moya, A.; Fresno, F.; Collado, L.; Vilatela, J.J.; de la Peña O'Shea, V.A. Hierarchical TiO_2 Nanofibres as Photocatalyst for CO_2 Reduction: Influence of Morphology and Phase Composition on Catalytic Activity. *J. CO2 Util.* **2016**, *15*, 24–31. [CrossRef]
8. Collado, L.; Reñones, P.; Fermoso, J.; Fresno, F.; Garrido, L.; Pérez-Dieste, V.; Escudero, C.; Hernández-Alonso, M.D.; Coronado, J.M.; Serrano, D.P.; et al. The role of the surface acidic/basic centers and redox sites on TiO_2 in the photocatalytic CO_2 reduction. *Appl. Catal. B Environ.* **2022**, *303*, 120931. [CrossRef]
9. Humayun, M.; Khan, A.; Luo, W. Modification strategies of TiO_2 for potential applications in photocatalysis: A critical review. *Green Chem. Lett. Rev.* **2018**, *2*, 86–102. [CrossRef]
10. Cortes, M.A.L.R.M.; Hamilton, J.W.J.; Sharma, P.K.; Brown, A.; Nolan, M.; Gray, K.A.; Byrne, J.A. Formal Quantum Efficiencies for the Photocatalytic Reduction of CO_2 in a Gas Phase Batch Reactor. *Catal. Today* **2019**, *326*, 75–81. [CrossRef]

11. Xi Chen, F.J.; Xi Chen, F.J. Photocatalytic Reduction of Carbon Dioxide by Titanium Oxide-Based Semiconductors to Produce Fuels. *Front. Energy* **2019**, *13*, 207–220. [CrossRef]
12. Chen, D.; Zhang, X.; Lee, A.F. Synthetic Strategies to Nanostructured Photocatalysts for CO_2 Reduction to Solar Fuels and Chemicals. *J. Mater. Chem. A* **2015**, *3*, 14487–14516. [CrossRef]
13. Fresno, F.; Jana, P.; Reñones, P.; Coronado, J.M.; Serrano, D.P.; de la Peña O'Shea, V.A. CO_2 Reduction over $NaNbO_3$ and $NaTaO_3$ Perovskite Photocatalysts. *Photochem. Photobiol. Sci.* **2017**, *16*, 17–23. [CrossRef] [PubMed]
14. Xu, F.; Meng, K.; Cheng, B.; Wang, S.; Xu, J.; Yu, J. Unique S-Scheme Heterojunctions in Self-Assembled TiO_2 /$CsPbBr_3$ Hybrids for CO_2 Photoreduction. *Nat. Commun.* **2020**, *11*, 4613. [CrossRef]
15. Zhong, J.; Li, J.; Zeng, J.; He, X.; Huang, S.; Jiang, W.; Li, M. Enhanced Photocatalytic Activity of In_2O_3-Decorated TiO_2. *Appl. Phys. A* **2014**, *115*, 1231–1238. [CrossRef]
16. Mu, J.; Chen, B.; Zhang, M.; Guo, Z.; Zhang, P.; Zhang, Z.; Sun, Y.; Shao, C.; Liu, Y. Enhancement of the Visible-Light Photocatalytic Activity of In_2O_3–TiO_2 Nanofiber Heteroarchitectures. *ACS Appl. Mater. Interfaces* **2012**, *4*, 424–430. [CrossRef]
17. Li, Y.; Yang, H.; Tian, J.; Hu, X.; Cui, H. Synthesis of In_2O_3 Nanoparticle/TiO_2 Nanobelt Heterostructures for near Room Temperature Ethanol Sensing. *RSC Adv.* **2017**, *7*, 11503–11509. [CrossRef]
18. Wang, H.; Wu, D.; Liu, C.; Guan, J.; Li, J.; Huo, P.; Liu, X.; Wang, Q.; Yan, Y. Fabrication of Ag/In_2O_3/TiO_2/HNTs Hybrid-Structured and Plasma Effect Photocatalysts for Enhanced Charges Transfer and Photocatalytic Activity. *J. Ind. Eng. Chem.* **2018**, *67*, 164–174. [CrossRef]
19. Gao, Y.; Qian, K.; Xu, B.; Li, Z.; Zheng, J.; Zhao, S.; Ding, F.; Sun, Y.; Xu, Z. Recent Advances in Visible-Light-Driven Conversion of CO_2 by Photocatalysts into Fuels or Value-Added Chemicals. *Carbon Resour. Convers.* **2020**, *3*, 46–59. [CrossRef]
20. Khan, M.M.; Ansari, S.A.; Pradhan, D.; Ansari, M.O.; Han, D.H.; Lee, J.; Cho, M.H. Band Gap Engineered TiO_2 Nanoparticles for Visible Light Induced Photoelectrochemical and Photocatalytic Studies. *J. Mater. Chem. A* **2013**, *2*, 637–644. [CrossRef]
21. Zhou, X.; Wu, J.; Li, Q.; Zeng, T.; Ji, Z.; He, P.; Pan, W.; Qi, X.; Wang, C.; Liang, P. Carbon Decorated In_2O_3/TiO_2 Heterostructures with Enhanced Visible-Light-Driven Photocatalytic Activity. *J. Catal.* **2017**, *355*, 26–39. [CrossRef]
22. Chen, Y.-C.; Pu, Y.-C.; Hsu, Y.-J. Interfacial Charge Carrier Dynamics of the Three-Component In_2O_3–TiO_2–Pt Heterojunction System. *J. Phys. Chem. C* **2012**, *116*, 2967–2975. [CrossRef]
23. Wang, H.; Ma, D.; Huang, X.; Huang, Y.; Zhang, X. General and Controllable Synthesis Strategy of Metal Oxide/TiO_2 Hierarchical Heterostructures with Improved Lithium-Ion Battery Performance. *Sci. Rep.* **2012**, *2*, 1–8. [CrossRef] [PubMed]
24. Wei, L.; Yu, C.; Zhang, Q.; Liu, H.; Wang, Y. TiO_2-Based Heterojunction Photocatalysts for Photocatalytic Reduction of CO_2 into Solar Fuels. *J. Mater. Chem. A* **2018**, *6*, 22411–22436. [CrossRef]
25. Fresno, F. Heterojunctions: Joining different semiconductors. *Green Energy Technol.* **2013**, *71*, 311–327.
26. Reñones, P.; Fresno, F.; Fierro, J.L.G.; de la Peña O'Shea, V.A. Effect of La as Promoter in the Photoreduction of CO_2 Over TiO_2 Catalysts. *Top. Catal.* **2017**, *60*, 1119–1128. [CrossRef]
27. Sreethawong, T.; Ngamsinlapasathian, S.; Yoshikawa, S. Photochemically deposited nano-Ag/sol–gel TiO_2–In_2O_3 mixed oxide mesoporous-assembled nanocrystals for photocatalytic dye degradation. *J. Colloid Interf. Sci.* **2014**, *421*, 191–198. [CrossRef] [PubMed]
28. Zhang, X.; Li, L.; Zhou, Q.; Cao, Y.; Ma, F.; Li, Y. Three-dimensionally ordered hollow sphere array Pt/In_2O_3–TiO_2 with improved photocatalytic efficiency. *New J. Chem.* **2019**, *43*, 10689–10698. [CrossRef]
29. Debeila, M.A.; Wells, R.P.K.; Anderson, J.A. Influence of Water and Pretreatment Conditions on CO Oxidation over Au/TiO_2–In_2O_3 Catalysts. *J. Catal.* **2006**, *239*, 162–172. [CrossRef]
30. Kaihang, S.; Fan, Z.; Ye, J.; Yan, J.; Ge, Q.; Li, Y.; He, W.; Yang, W.; Liu, C.-J. Hydrogenation of CO_2 to methanol over In_2O_3 catalyst. *J. CO2 Util.* **2015**, *12*, 1–6.
31. Yang, X.; Wang, Y.; Xu, L.; Yu, X.; Guo, Y. Silver and Indium Oxide Codoped TiO_2 Nanocomposites with Enhanced Photocatalytic Activity. *J. Phys. Chem. C* **2008**, *112*, 11481–11489. [CrossRef]
32. Tahir, B.; Tahir, M.; Saidina, A.; Nor, A. Gold–indium modified TiO_2 nanocatalysts for photocatalytic CO_2 reduction with H_2 as reductant in a monolith photoreactor. *Appl. Surf. Sci.* **2015**, *338*, 1–14. [CrossRef]
33. Tahir, M.; Amin, N.A.S. Indium-Doped TiO_2 Nanoparticles for Photocatalytic CO_2 Reduction with H_2O Vapors to CH_4. *Appl. Catal. B Environ.* **2015**, *162*, 98–109. [CrossRef]
34. Guo, J.; Ouyang, S.; Kako, T.; Ye, J. Mesoporous $In(OH)_3$ for Photoreduction of CO_2 into Renewable Hydrocarbon Fuels. *Appl. Surf. Sci.* **2013**, *280*, 418–423. [CrossRef]
35. Hu, B.; Guo, Q.; Wang, K.; Wang, X. Enhanced Photocatalytic Activity of Porous In_2O_3 for Reduction of CO_2 with H_2O. *J. Mater. Sci. Mater. Electron.* **2019**, *30*, 7950–7962. [CrossRef]
36. García, L.M.P.; Lovisa, L.X.; Gurgel, G.H.M.; Nascimento, R.M.; Paskocimas, C.A.; Motta, F.V.; Bomio, M.R.D. Influence of the Number of Layers and Crystallization Temperature on the Photocatalytic Activity of TiO_2/In_2O_3 Thin Films. *Mater. Sci. Eng. Int. J.* **2017**, *1*, 22–28. [CrossRef]
37. Hoch, L.B.; He, L.; Qiao, Q.; Liao, K.; Reyes, L.M.; Zhu, Y.; Ozin, G.A. Effect of Precursor Selection on the Photocatalytic Performance of Indium Oxide Nanomaterials for Gas-Phase CO_2 Reduction. *Chem. Mater.* **2016**, *28*, 4160–4168. [CrossRef]
38. Pan, Y.-X.; You, Y.; Xin, S.; Li, Y.; Fu, G.; Cui, Z.; Men, Y.-L.; Cao, F.-F.; Yu, S.-H.; Goodenough, J.B. Photocatalytic CO_2 Reduction by Carbon-Coated Indium-Oxide Nanobelts. *J. Am. Chem. Soc.* **2017**, *139*, 4123–4129. [CrossRef] [PubMed]

39. Collado, L.; Jana, P.; Sierra, B.; Coronado, J.M.; Pizarro, P.; Serrano, D.P.; de la Peña O'Shea, V.A. Enhancement of Hydrocarbon Production via Artificial Photosynthesis Due to Synergetic Effect of Ag Supported on TiO_2 and ZnO Semiconductors. *Chem. Eng. J.* **2013**, *224*, 128–135. [CrossRef]
40. Zhang, J.; Li, M.; Feng, Z.; Chen, J.; Li, C. UV Raman Spectroscopic Study on TiO_2. I. Phase Transformation at the Surface and in the Bulk. *J. Phys. Chem. B* **2006**, *110*, 927–935. [CrossRef] [PubMed]
41. Kelly, S.; Pollak, F.H.; Tomkiewicz, M. Raman Spectroscopy as a Morphological Probe for TiO_2 Aerogels. *J. Phys. Chem. B* **1997**, *101*, 2730–2734. [CrossRef]
42. Chong, S.K.; Azizan, S.N.A.; Chan, K.W.; Nguyen, H.-Q.; Chiu, W.S.; Aspanut, Z.; Dee, C.F.; Rahman, S.A. Structure Deformation of Indium Oxide from Nanoparticles into Nanostructured Polycrystalline Films by in Situ Thermal Radiation Treatment. *Nanoscale Res. Lett.* **2013**, *8*, 428. [CrossRef] [PubMed]
43. Gan, J.; Lu, X.; Wu, J.; Xie, S.; Zhai, T.; Yu, M.; Zhang, Z.; Mao, Y.; Wang, S.C.I.; Shen, Y.; et al. Oxygen Vacancies Promoting Photoelectrochemical Performance of In_2O_3 Nanocubes. *Sci. Rep.* **2013**, *3*, 1021. [CrossRef] [PubMed]
44. Berengue, O.; Rodrigues, A.; Dalmaschio, C.; Lanfredi, A.; Leite, E.; Chiquito, J. Structural characterization of indium oxide nanostructures: A Raman analysis. *J. Phys. D Appl. Phys.* **2010**, *43*, 45401. [CrossRef]
45. Panneerdoss, I.J.; Jeyakumar, S.J.; Ramalingam, S.; Jothibas, M. Characterization of Prepared In_2O_3 Thin Films: The FT-IR, FT-Raman, UV-Visible Investigation and Optical Analysis. *Spectrochim. Acta. A Mol. Biomol. Spectrosc.* **2015**, *147*, 1–13. [CrossRef]
46. Garcia, L.M.P.; Tavares, M.T.S.; Andrade Neto, N.F.; Nascimento, R.M.; Paskocimas, C.A.; Longo, E.; Bomio, M.R.D.; Motta, F.V. Photocatalytic Activity and Photoluminescence Properties of TiO_2, In_2O_3, TiO_2/In_2O_3 Thin Films Multilayer. *J. Mater. Sci. Mater. Electron.* **2018**, *29*, 6530–6542. [CrossRef]
47. Liqiang, J.; Yichun, Q.; Baiqi, W.; Shudan, L.; Baojiang, J.; Libin, Y.; Wei, F.; Honggang, F.; Jiazhong, S. Review of Photoluminescence Performance of Nano-Sized Semiconductor Materials and Its Relationships with Photocatalytic Activity. *Sol. Energy Mater. Sol. Cells* **2006**, *90*, 1773–1787. [CrossRef]
48. Garcia-Muñoz, P.; Fresno, F.; Ivanez, J.; Robert, D.; Keller, N. Activity enhancement pathways in $LaFeO_3$@TiO_2 heterojunction photocatalysts for visible and solar light driven degradation of myclobutanil pesticide in water. *J. Hazard. Mater.* **2020**, *400*, 123099. [CrossRef]
49. Thompson, W.; Sanchez Fernandez, E.; Maroto-Valer, M. Review and Analysis of CO_2 Photoreduction Kinetics. *ACS Sustain. Chem. Eng.* **2020**, *8*, 4677–4692. [CrossRef]
50. Liu, L.; Zhao, C.; Pitts, D.; Zhao, H.; Li, Y. CO_2 Photoreduction with H_2O Vapor by Porous MgO–TiO_2 Microspheres: Effects of Surface MgO Dispersion and CO_2 Adsorption–Desorption Dynamics. *Catal. Sci. Technol.* **2014**, *4*, 1539–1546. [CrossRef]